Tailoring silk fibroin separator membranes pore size for improving performance of lithium ion batteries

Ander Reizabal[1,2], R. Gonçalves[3], A. Fidalgo-Marijuan[1,4], C. M. Costa[3,5,*], Leyre Pérez[1,2], Jose-Luis Vilas[1,2], S. Lanceros-Mendez[1,6,*]

[1]BCMaterials, Basque Center for Materials, Applications and Nanostructures, UPV/EHU Science Park, 48940 Leioa, Spain.

[2]Macromolecular Chemistry Research Group (LABQUIMAC). Dept. of Physical Chemistry. Faculty of Science and Technology. University of the Basque Country (UPV/EHU), Spain.

[3]Center of Chemistry, University of Minho, 4710-058 Braga, Portugal

[4]Dept. of Mieralogy and Petrology, University of the Basque Country (UPV/EHU), Barrio Sarriena s/n, Leioa, Bizkaia 48940, Spain

[5]Center of Physics, University of Minho, 4710-058 Braga, Portugal

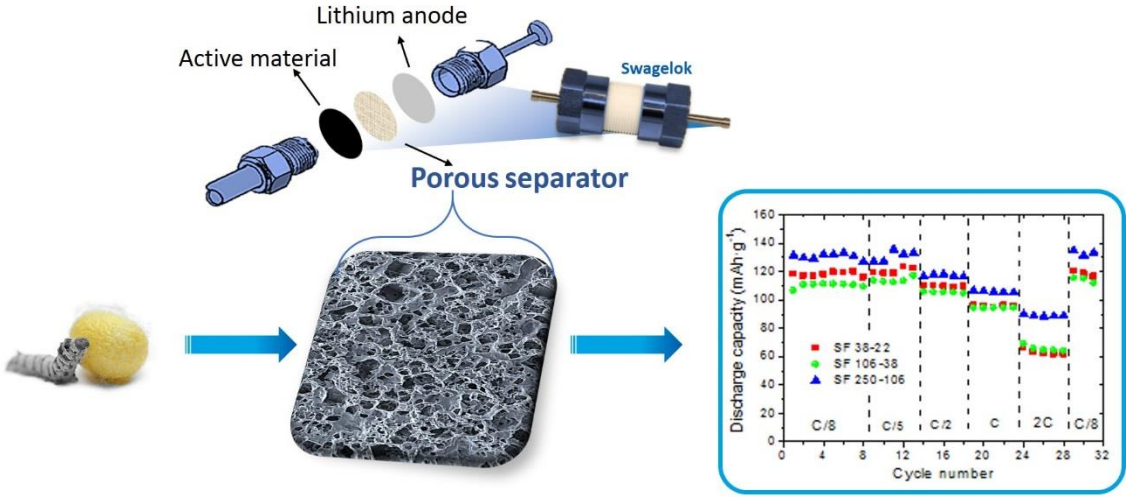
[6]Ikerbasque, Basque Foundation for Science, 48013 Bilbao, Spain

[*]**Corresponding Authors** Email: C. M. Costa (cmscosta@fisica.uminho.pt); S. Lanceros-Méndez (senentxu.lanceros@bcmaterials.net)

Abstract:

The search of natural materials for their application in energy storage systems in general and batteries in particular is growing due to their promising properties and the need of environmental sustainability. Silk fibroin (SF) is one of those materials due to their mechanical and thermal properties, non-toxicity and biocompatibility. Further, SF exhibits excellent cycling performance as separator for lithium-ion battery applications. This work reports on SF membranes with different pore sizes (within the rages: 38-22, 106-38 and 250-106 μm) prepared for separators in lithium-ion batteries. The morphology, structure and thermal properties were evaluated. It is shown that the β-sheet conformation percentage increases with increasing pore size, which also leads to higher electrolyte uptake, reaching 350% for SF membranes with pore size of 250-106 μm. With respect to battery performance, a high discharge capacity (131.3 mAh g^{-1}, for C/8) is obtained for this membrane.

Graphical abstract



Keywords: silk fibroin; pore size control; separator membrane; lithium-ion battery

1. Introduction

Renewable energy sources are essential for improving the sustainability of the earth resources, given by the increase of global population as well as the dependence on natural gas and fossil fuels, which should be reduced in the next years considering global warming [1, 2].

Batteries are essential elements for storing the energy obtained from renewable systems, in particular, lithium-ion batteries play an important role based on their higher energy and power density in comparison with other battery systems, such as lead acid and nickel metal hydride batteries (NiMH) [3]. Further, lithium-ion batteries are increasingly used in many applications such as consumer electronics, medical applications and electrical vehicles, being the battery type most used in the world with high potential growth [4]. The main issues that should be improved with respect to lithium-ion batteries are their energy density and power, materials availability, safety and cost [5]. A relevant issue is the use of materials with benign environmental properties and low human health impacts. New materials should be done for improving safety and producing more sustainable lithium-ion battery systems [6, 7] for all components: electrodes and separator/electrolyte [8].

The electrodes correspond to the anode (negative electrode) that should show low potential to provide a high cell voltage, and the cathode (positive electrode) which determines the battery capacity [4]. In relation to the separator, it is localized between both electrodes and serves as the medium for transfer of lithium-ions during the charge and discharge processes [9]. The separator is typically constituted by a polymeric membrane soaked in the electrolyte solution, i.e, a liquid electrolyte where salts are dissolved in water or organic solvents, [9]. Typically, the polymeric matrix is based on poly(ethylene) (PE) [10], poly(propylene) (PP) [10], poly(ethylene oxide) (PEO) [11], poly(acrylonitrile) (PAN) [12], poly (methyl methacrylate) (PMMA) [13], and poly(vinylidene fluoride) (PVDF) [9, 14] and its copolymers poly(vinylidene fluoride-co-trifluoroethylene) (P(VDF-TrFE)) [15], poly(vinylidene fluoride-co-hexafluoropropylene), (P(VDF-HFP)) [16], and poly(vinylidene fluoride-co-chlorotrifluoroethylene), (P(VDF-CTFE)) [17]. Considering the environmental impact of these synthetic polymers, conventional separators are substituted by natural polymers, such as cellulose [18], lignin [19], polyimide [20] and silk fibroin (SF) [21], contributing to the reduction of the environmental impact of lithium-ion batteries [22].

In particular, SF is composed by repetitive sections of glycine (45%), alanine (30%), and serine (12%) in a ratio of approximately 3: 2: 1 and is dominated by [Gly-Ala-Gly-Ala-Gly-Serl]$_n$ sequences with β-sheet crystallites and amorphous domains.

XXX

The main advantages for SF for battery applications are its non-toxicity, mechanical flexibility, as well as excellent thermal properties and suitable ionic conductivity [23, 24]. SF also exhibits excellent cycling performance as separator for lithium-ion batteries [21]. SF can be obtained from *Bombyx mori* silkworm cocoons where the fibroin protein shows a semi crystalline structure and represents 72-81% of total mass [25-27].

The correlation between the fraction of β-sheet conformations and the ionic conductivity of SF membranes has been demonstrated [21], as well as its suitability for energy storage. Thus, SF is beginning to be used in the field of solid state electrochemistry devices such as, Mg–Air bioelectric batteries [28], lithium-sulfur batteries [29], magnesium primary batteries [30], lithium-oxygen batteries [31] and anode electrodes [32].

It has been also shown that the degree of porosity affects the wettability process of the electrolyte solution and consequently the ionic conductivity, some authors indicate that there exists a limit value that and should be around 40% depending on the polymer matrix type [33, 34].

Considering that the separator's pore structure is a critical design parameter that affects the true length of the ionic path (tortuosity), the goal of the present work is to prepare porous membranes based on SF, through the solvent casting salt leaching method with the same degree of porosity but different pore size, allowing to optimize the performance of SF separator membranes. Further, the processing method is highly reproductive, scalable and low cost and allows to obtain three-dimensional separators with interconnected pores and sizes ranging from 22 to 250 μm, maintaining the necessary mechanical stability.

The morphology, polymer phase, thermal and mechanical properties, contact angle and uptake value were analyzed for the different SF separators, as well as the electrochemical properties. The results show a correlation between pore size, β-sheet conformation and discharge capacity value for the prepared SF separators, corroborating its applicability as separator at lithium-ion battery systems.

2. Experimental details

2.1. Materials

Bombyx mori cocoons were supplied by APPACDM from Castelo Branco (Portugal). Formic acid and sodium chloride (NaCl) were provided by Sigma Aldrich with a 98.9% of purity. Poly(vinylidene fluoride) (PVDF, Solef 5130, Mw=1000-1300 kDa), C-$LiFePO_4$ (LFP), and carbon black (Super P-C45) were acquired from Solvay, Phostech Lithium and Timcal Graphite & Carbon, respectively. The solvent *N,N'*-dimethylpropyleneurea (DMPU), the conventional electrolyte 1M $LiPF_6$ in ethylene carbonate-dimethyl carbonate (EC-DMC, 1:1 vol) were purchased from LaborSpirit and Solvionic, respectively.

2.2. Porous membranes preparation

Figure 1 shows the main processing steps for obtaining SF membranes with different pore size.

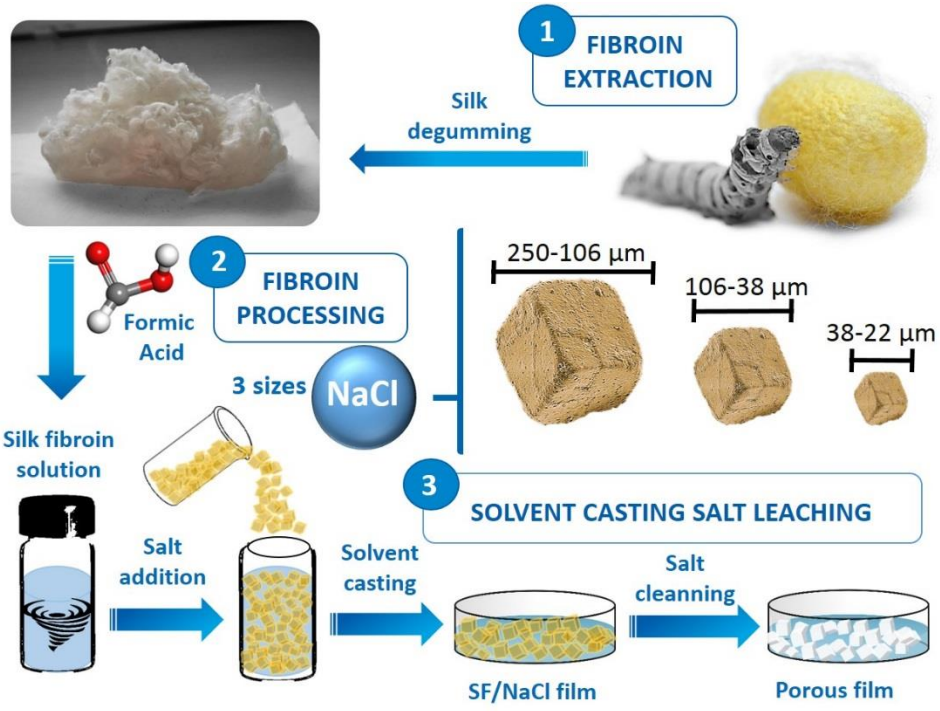


Figure 1 – Main processing steps for porous SF membranes preparation.

After worms removing, cocoons from *Bombyx Mori* silkworms were cleaned and cut into small pieces. The sericin of the cocoons was removed by boiling the cut pieces in a 0.2 M Na_2CO_3 solution for 5 minutes. 40 ml of aqueous Na_2CO_3 solution were used per

gram of raw silk degumming. The obtained SF fibers were cleaned by distilled water and dried at room temperature during 24 h. SF was then unraveled and dissolved in a formic acid/$CaCl_2$ 0.2 M solution with 10 ml formic acid (FA) per gram of SF. In order to remove insoluble residues, the solution was centrifuged at 7,500 rpm and then casted in polyethylene petri dishes. Completely dried membranes were then immersed into distilled water bath to remove the $CaCl_2$. To ensure the complete removing of salts, continuous water changes were performed until the water solution showed a constant electrical conductivity. $CaCl_2$ free SF films, were finally dried at room temperature until constant weight was obtained.

Porous membranes were prepared by a salt leaching method. For that, the previously prepared pure SF was initially dissolved in FA by magnetic stirring (20 ml formic acid per gram of SF). After complete dissolution, well sifted NaCl particles in a proportion of 1:10 (w:w) SF:salt (always keeping constant the salt weight), were added to the solution. Sifted NaCl was divided into 3 different size ranges in order to produce membranes with variable porous sizes: 250-106 µm, 106-38 µm and 38-22 µm (Figure 1). Based on the sizes, the resulting membranes were named as SF 205-106, SF 106-38 and SF 38-22. After a few minutes of energetic stirring, a homogeneous mixture was obtained. The resulting solution containing dissolved SF and dispersed NaCl was poured over polyethylene petri dishes and dried until complete evaporation of the solvent.

The obtained SF/NaCl composites were finally washed by distilled water bath at room temperature to eliminate the non-desirable NaCl. After several water changes, the solution shows constant electrical conductivity values showing the completely removing of NaCl. The obtained porous membranes were placed in an airing chamber and dried for 24h.

2.3. Characterization techniques

Morphological analysis*:* In order to analyze the microstructure of the samples, porous membranes were characterized by scanning electron microscope (SEM, NanoSEm – FEI Nova 200 (FEG/SEM)) with an accelerating voltage of 15 kV. The membranes were previously coated by a conductive gold layer by sputtering with a Polaron SC502 apparatus. Cross section images were taken in cryogenically fractured samples.

***Infrared spectroscopy**:* Samples secondary structure analysis was performed by Fourier Transformed Infrared Spectroscopy (FTIR) with a Jasco FT/IR-4100 system. FTIR spectra were collected in the ATR mode from 4000 to 600 cm^{-1} after 64 scans with a resolution of 4 cm^{-1}. In order to determine the vibrational band assignment of each sample, all the scans were normalized with Amide II. Then spectral region corresponding to Amide I was carried out following the previously reported methodology with the OriginPro 8.1 software (OriginLab, Northampton) [35].

Thermal and mechanical analysis: Thermal degradation and heating transitions were determined by Thermogravimetric Analysis (TGA) and Differential Scanning Calorimetry (DSC), respectively.

Samples thermal degradation was measured with a TA/SDTA 851e Metter Toledo apparatus under air flow of 50 mL min^{-1} operating between 25 and 800 °C at 10 °C min^{-1}. DSC was performed with a Mettler Toledo DSC 822e under nitrogen flow of 20 $mL \cdot min^{-1}$ operating between 25 to 350 °C at 20 °C min^{-1}. Before the measurements, samples were treated by dynamical heating from 25 to 168ºC for remaining solvent evaporation.

Samples tensile properties were analyzed in 400 µm thick, 5 mm wide and 15 mm long samples with a Metrotech MTE-1 from Techlab systems at a stretching speed of 10 mm min^{-1}. Specimens were stretched at room temperature until breaking. Young's modulus (E') was determined from the slope between 1.5 and 2.5% strain in the stress-strain plot. Reported values represent mean average values and standard deviations (3 specimens were measured for each material).

Solvent affinity: The affinity between the electrolyte (1M $LiPF_6$ in EC: DMC, 1:1 vol.) and the membranes was measured by contact angle and uptake.

Wettability of the SF porous membranes was measured by the formed contact angle between water and/or electrolyte solution and the membrane surface. 200 µl drops were deposited on a flat surface and the contact angle of the droplet with the surface was measured. No change in the contact angle during the measurement period was observed. 10 measurements per sample were performed at different points of the samples and the average value was calculated.

Samples ability to uptake electrolyte was obtained by immersing the membranes into the electrolyte solution (1M $LiPF_6$ in EC: DMC, 1:1 vol.) over time, through the following equation:

$$uptake\ (\%) = \frac{m_i - m_0}{m_0} \times 100 \quad (1)$$

where m_0 is the weight of the dry membrane and m_i is the weight of the membrane after immersion in the electrolyte solution.

SF membranes characterization results were compared with neat SF films in order to give a close understanding of the physical-chemical changes occurring in SF as result of salt leaching process.

Porosimetry and surface area determination: Porosimetry and surface area determination were carried out by mercury intrusion porosimetry (MIP) in a Quantachrome Instruments Poremaster-60 GT operating in the pressure range from vacuum (10^{-4} MPa) to 414 MPa. Samples were degassed *in situ* at 120 ºC during 12 h prior to measurement. A contact angle of 140º and a surface tension of 480 dyn·cm^{-1} for mercury and a pressure equilibration time of 11 s were used. Before the measurement of MIP the He gas density for all the samples were measured in a Quantachrome Instruments automatic Micro Ultrapycnometer.

2.4. Electrochemical characterization

Impedance spectroscopy measurements were carried out into SF membranes immersed of the conventional electrolyte 1M $LiPF_6$ in ethylene carbonate-dimethyl carbonate (EC-DMC, 1:1 vol.) for 15 minutes. Measurements were performed in steel/membrane/steel symmetrical cells, at room temperature, in the frequency range between 10 mHz and 1 MHz with an amplitude of 10 mV with a Biologic VMP3 instrument. The ionic conductivity (σ_i) of the SF separators was calculated by the following equation:

$$\sigma_i = \frac{d}{R_b * A} \quad (2)$$

where R_b is the bulk resistance, d is the thickness and A is the area of the sample.

The R_b is obtained from the intercept of the imaginary impedance (minimum value of Z'') with the slanted line in the real impedance (Z') [36].

Another relevant parameters such as tortuosity (τ) and MacMulin number (N_M) of the SF membranes were calculated through the following equations:

$$\tau = \sqrt{\frac{\sigma_0 \varepsilon}{\sigma_i}} \quad (3)$$

$$N_M = \frac{\sigma_0}{\sigma_i} \quad (4)$$

where σ_0 is the electrical conductivity of the pure electrolyte solution (10.07 $mS \cdot cm^{-1}$), σ_i is the conductivity of the membrane plus the electrolyte solution and ε is the degree of porosity of the SF membrane.

2.5. Cathode preparation

The cathode was prepared using 80 wt.% C-$LiFePO_4$, 10 wt.% carbon black and 10 wt.% PVDF in 2.25 mL of DMPU for 1g of solid material. More details on the electrode preparation are reported in [37]. The resulting slurry was then casted on aluminum foil by doctor-blade technique and dried at 80 ºC for 2 h. The thickness and porosity of the cathode electrodes are 20 μm and 60%, respectively.

2.6. Lithium cell preparation and electrochemical performance

Swagelok type Li/C-$LiFePO_4$ half-cells were assembled in an argon-filled glove box where O_2 and H_2O levels were kept bellow 0.1 ppm and SF membranes were incorporated as separators (10 mm diameter) soaked in electrolyte solution as represented in Figure 2.

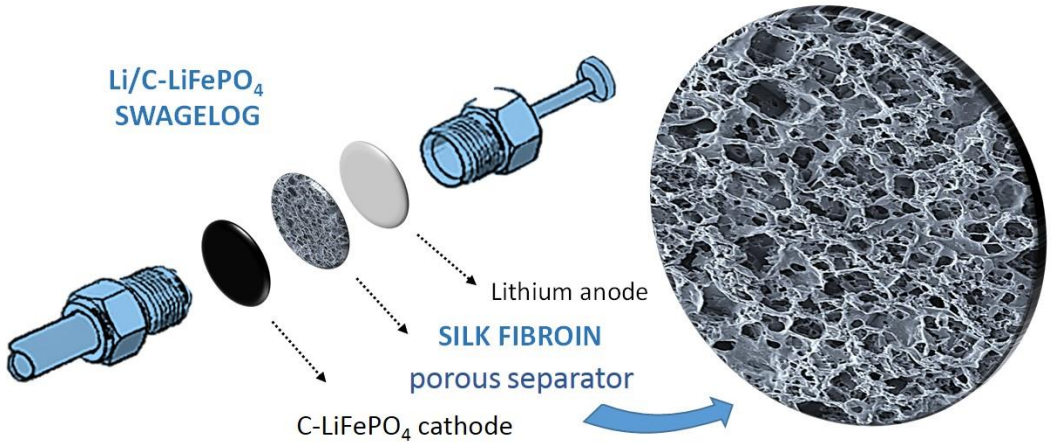


Figure 2 – Schematic representation of the Swagelok cell type and its components.

Metallic lithium (8 mm diameter) was used as anode and the C-$LiFePO_4$ based electrode as cathode (8 mm diameter). Charge-discharge tests were obtained at room temperature in the voltage range from 2.5 to 4.2 V at current rates from C/5 to 2C (C = 170 mAh g^{-1}) using a Biologic VMP3 instrument.

The electrical properties of the Li/C-$LiFePO_4$ half-cells were measured by electrochemical impedance spectroscopy (EIS) with a Biologic VMP3 instrument, in the frequency range from 10 mHz to 1 MHz, with an amplitude of 10 mV AC voltage signal.

3. Results and Discussion

3.1.Membranes morphological parameters.

Battery separators performance is strongly dependent on membranes morphological parameters such as pore size, thickness, porosity and pores interconnectivity [38]. SEM images allow a precise determination of membranes morphology and enable the determination of pores dimensions and membranes thickness. SF membranes cross section, up surface and down surface were evaluated and are summarized in Figure 3.

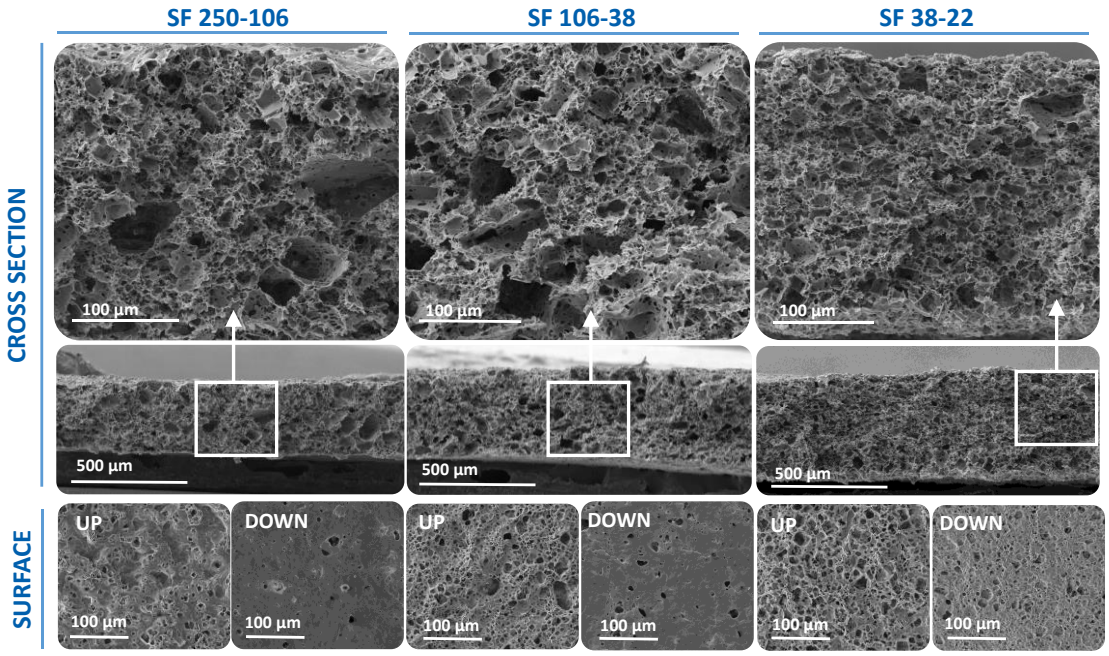


Figure 3 – SEM micrographs cross section, up surface and down surface of a) SF 250-106 µm, b) SF 106-38 µm and c) SF 38-22 µm porous membranes.

As can be observed in cross section SEM images, in contrast with the flat and non-porous morphology of SF films obtained from solvent casting [39], those membranes obtained by salt leaching process result in structures with a well-defined porous morphology. In agreement with the used salt crystal sizes, the pores average dimensions decrease with salt size decrease, thus SF 250-106 μm membrane presents the biggest porous size, followed by SF 106-38 μm membrane and SF 38-22 μm membrane. The observed pores show a wide distribution of sizes and forms as the observed pores represent a single section of the irregular pores. The complete cross section images show the uniform pores distribution and the constant thickness of membranes, which confirms the effectivity of the methodology to produce porous SF membranes. Even when the same amount of salt was used for the preparation of the membranes, a visible variation of thickness can be observed. Thus, SF 250-160 μm, SF 160-38 μm and SF 38-22 μm membranes present a thickness of 330, 390 and 445 μm. This effect is due to the increasing number of pores existing in the same matrix with decreasing salt average size. Each pore corresponds with a salt particle which is completely surrounded by SF. Both surfaces (upper and lower) present a porous morphology, nevertheless due to the solvent evaporation method each surface are slightly different. The lower surface was in contact with the petri dishes, resulting in a flat and less porous surface compared with the upper face. However, the obtained pore sizes will provide enough space for the electrolyte adsorption ensuring the fast lithium-ion percolation through the separator while preventing short-circuit and self-discharge.

Mercury intrusion porosimetry (BET) was used in order to determine the total porosity and the surface area of the SF membranes. As expected, the results confirm that the total porosity is quite similar for all samples, unless the SF 250-106 μm that presents the highest total porosity and surface area, while for the SF 106-38 μm and SF 38-22 μm the values decrease (Table 1).

Table 1 – Total porosity (%) and surface area ($m^2 \cdot g^{-1}$) of the SF 250-106 μm, SF 106-38 μm and SF 38-22 μm porous samples.

	Total Porosity (%)	Surface area ($m^2 \cdot g^{-1}$)
SF 38-22 μm	80,67	54,50
SF 106-38 μm	82,55	66,40
SF 250-106 μm	86,03	69,74

3.2. *Membranes physical-chemical characterization*

The SF chains arrangements can show different conformations depending on the processing method and conditions [21]. To evaluate these conformations a FTIR-ATR spectra analysis was performed (Figure 4a). The main protein secondary polymorph crystalline structures of SF are silk I, II and III [40]. Each one of these crystalline structures represent: silk I – metastable state between α-helix and the β-sheet partially ordered structure; silk II – antiparallel β-sheet structure; silk III – formed at air-liquid interfaces. Silk II is the most stable structure and is typically present in pristine silk, typically leading to a random conformation in the SF regeneration [41].

The amide I band is characteristic of the SF secondary structure, the stretching vibration of carbonyl group being very sensitive to the specificity and magnitude of the formed hydrogen bonds. According to this, the deconvolution of the amide I band (Figure 4b) was performed in all samples. Five conformations can be found in the amide I at different frequency ranges: turn (T, 1696-1663 cm^{-1}), α-helices (A, 1662-1656 cm^{-1}), random coil (RC, 1655-1638 cm^{-1}), β-sheet (B, 1637-1616 cm^{-1} and 1705-1695 cm^{-1}) and side chain (SC, 1615-1605 cm^{-1}) [42]. According to the obtained results, the SF film presents 49.3 % of β-sheet and with the inclusion of the salt (38-22 μm), the percentage keeps almost the same (48.0 %). Increasing of the salt size, 106-38 and 250-106 μm, the β-sheet percentage increases to 65.1 % and 65.9 %, respectively. The results confirm that the pore size increase based on the inclusion of larger salt sizes leads to an increase in the β-sheet percentage with respect to SF films, fact which is attributed to the influence in the crystallization process based on surface interactions between the filler and the crystallizing SF. It is to notice that larger filler size also corresponds to a larger surface area (Table 1). It is also observed that the β-sheet percentage within the SF porous membranes is higher than the one obtained by those porous structures obtained from LiBr solutions [21]. The SF films display a profile of the amide I that contains 20.1 % of SC, 9.8 % of A, 10.3 % of T and 10.5 % of RC. With the addition of the salts 38-22 μm, the T (8.6 %) and A (11.9 %) content are maintained almost with the same percentage, but the RC increases to 19.0 % and the SC decreases to 12.4 %. Increasing

the salt size to 106-38 μm, leads to a considerable decrease of the RC (7.0 %), the T (11.9 %), A (8.2 %) and SC (7.7 %) keeping almost with the same percentage. Finally, SF 250-106 leads to a situation in which all the conformations present almost the same values T (10.8 %), A (8.2 %), RC (6.5 %) and SC (8.7 %). Thus, it is concluded that the inclusion of the salt with different sizes and the corresponding modifications in the crystallization conditions based on the different surface area (Table 1), leads to variations in the SF conformations content present in each sample [43].

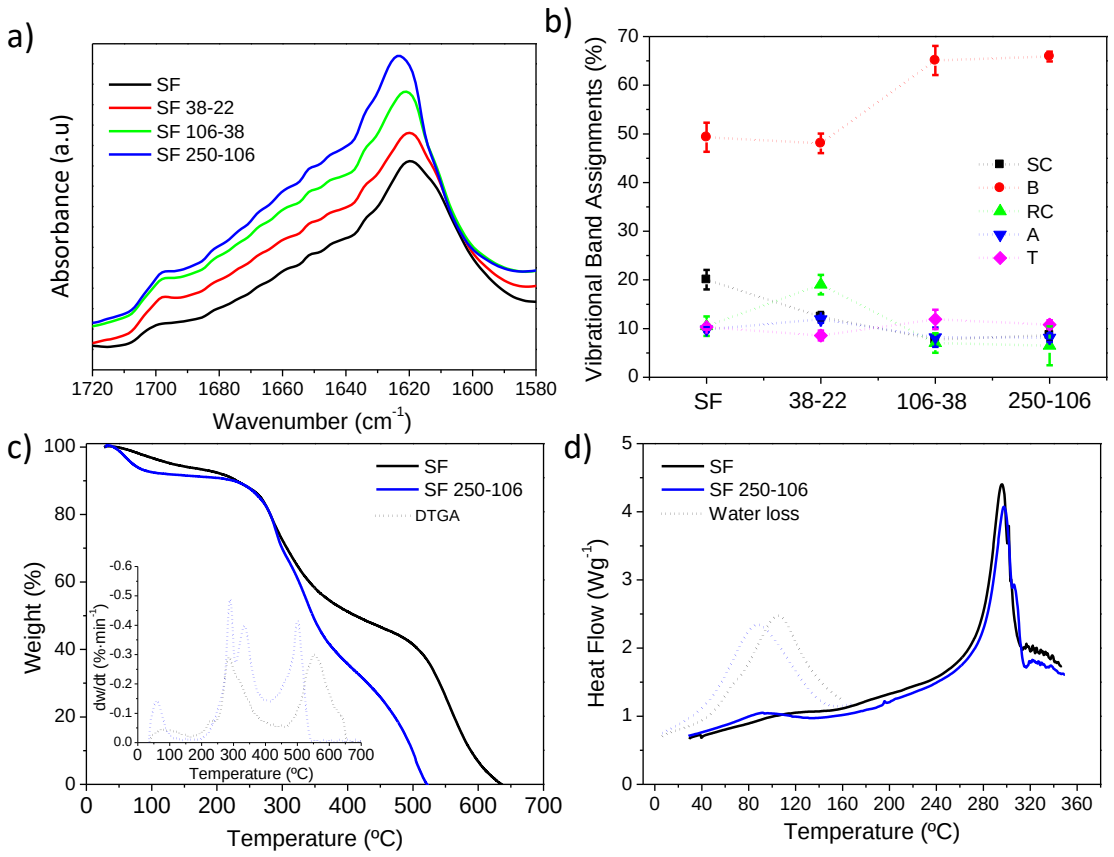


Figure 4 – SF film and SF membranes a) FTIR spectra, b) vibrational assignment of the different conformations of the silk amide I band, c) TGA (insert figure represent the DTGA) and d) DSC thermographs.

Thermal degradation and thermal transitions of SF porous membranes were studied by TGA and DSC techniques, respectively, and presented in Figure 4c and 4d. Due to the identical thermal behavior of the obtained SF membranes, SF 250-106 is presented as representative.

The thermal degradation of neat SF occurs in three main stages (Figure 4c). The first stage until 150°C is related to solvent removal (water + solvent), the second degradation

stage ranges from 200 ºC to 270 ºC and corresponds to the breakdown of side chain groups of amino acid residues as well as the cleavage of peptide bonds [39]. The final degradation step, observed above 550 ºC, is related with the combustion of the remaining organic compounds. The induced porosity by salt leaching triggers slight changes in SF thermal degradation process. As it can be observed, the first degradation peak, related with the removal of the solvent match in temperature with the one observed in the films. However, the intensity of the degradation increases, showing the enhanced ability of the porous membranes to hold back solvents or to absorb humidity from the ambient. The starting point of the second degradation stage of SF membranes also remains constant at 200 ºC with respect to the one of the films, being also in the same temperature range of separator membranes with excellent thermal stability and well above commonly used separators based on polyolefin [44].

Around 300 ºC SF membranes degradation process starts to accelerate. This effect remains during whole degradation process. This expected effect is attributed to the chaotropic effect of salt over the SF structure [45]. During the salt leaching process, salt crystals experience a slight dissociation process, which liberate free ions to de solution. Before solvent evaporation, these charged ions are able to interact with the still dissolved SF chains and produce small breaks into molecular chain. As a consequence, the more accessible side chain groups of amino acid residues as well as peptide bonds degrade more easily [46].

DSC curves (Figure 4d) reveal that, as observed in the thermal degradation process, the induced porosity into the SF membranes slightly affects the thermal transitions of the membranes. During the first thermal annealing, and in agreement with the thermal degradation results, neat SF shows an endothermic peak between 75 and 150 ºC attributable to solvent evaporation. During the second annealing process, the obtained peaks suggest the almost total solvents elimination [47]. No thermal transitions are observable until 260 ºC, which is related to the thermal degradation. The existence of the pores in the SF membranes just affects the endothermic peak observed during the first annealing, which is due to the increased surface area, as previously indicated. Thermal results confirm that no changes will occur during battery performance during the work temperatures range and even under uncontrolled heating.

Mechanical properties of the different samples were evaluated in order to verify the influence of the porosity in the mechanical properties of SF. From the stress-strain

curves (Figure 5a), ultimate tensile strength, elongation at break (ε_B) and Young's modulus (E) were calculated (Figure 5b).

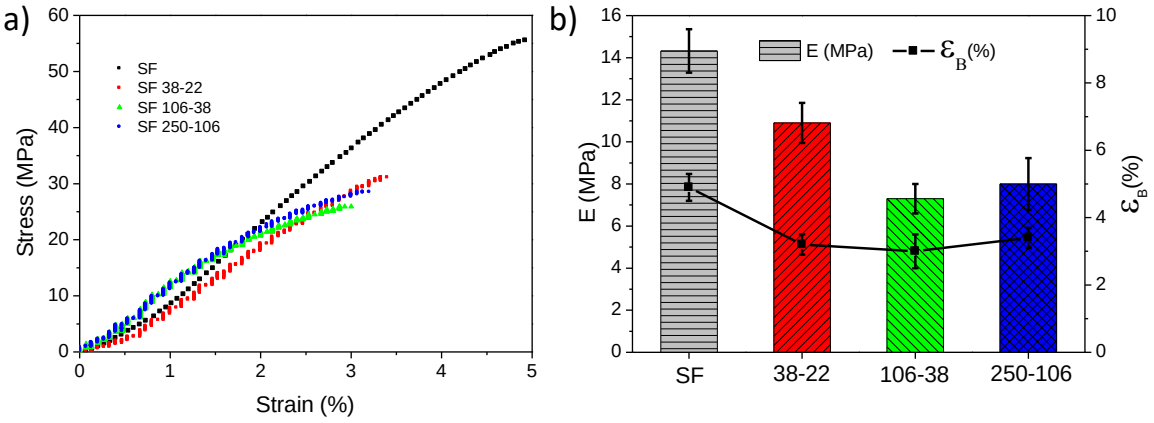


Figure 5 – a) Representative stress-strain plots and b) Young's modulus and elongation at break (ε_B), for the SF film and the SF samples with different porosities.

SF is composed by crystalized β-sheet nodes linked by amorphous domains and during the first elongation stages, amorphous domains unravel, storing the loaded force and giving to the structure elastic properties [48]. When linkers are completely stretched, the force happens to be supported by nodes, which no elongate [49]. H-bond that bonds β-sheets ordered structures are much weaker than the covalent forces that maintain the peptide chain connected. As a consequence, when loaded strength overpass the supported force by β-sheets the structure breaks. Nevertheless, the interconnected structure gives to the SF additional mechanical strength. After the individual β-sheets break, the loaded force is transmitted to the surrounding nodes along the cross-section [50]. As consequence, mayor amorphous composition gives to the SF mayor elastic properties and mayor crystalline structure gives higher loading strength abilities. Thus, and related with the FTIR results (Figure 4b), the highly ordered structure of SF leads to fully reversible linear viscoelastic behavior at low loading forces due to linkers elongation followed by brittle break due to the β-sheet nodes breaking process (Figure 5a). This advantageous secondary organization leads to loading stress up to 55 MPa and high elastic modulus. The same mechanical behavior is observed for SF membranes even their break becomes at lower loaded forces due to the decreased SF content by section. The effect of the porosity in the mechanical properties is higher than the effect of the variations in the secondary structure. As a consequence, the existence of the pores

reduces SF loading stress and elongation at break equally in all the porous membranes, independently of the average pore size. Despite of this reduction, the forces involved in battery assembly [51] (1 MPa) are lower than the elongation at break results, showing that these samples can be applied as separators in batteries systems. It is also to notice that the sample show the required mechanical flexibility, as shown in Figure 5c for the SF membrane with 106-38 μm pore size.

3.3. Contact angle, uptake, ionic conductivity value and impedance behavior

The contact angle was measured in order to evaluate the wettability of the membranes not only with water but also with the electrolyte solution. These measurements are essential to understand the surface characteristic of the samples. The contact angle between water and the prepared samples is illustrated in Figure 6a. The results show that the water contact angle between with the SF film surface is variable over time. In the first moments after water drop, the contact angle between SF and water is near 90º (85 ± 4). This behavior reveals a competition between the tendency of water to stick to itself [52] and to the SF surface as a result of the dual composition of SF based on hydrophobic domains of repetitive Gly-Ala-Gly-Ala-Gly-X (where X can be Ser or Tyr) hexapeptide sequence and non-repetitive hydrophilic domains [53]. Salt leaching process increases the amount of ordered hydrophobic domains in SF (see FTIR results, Figure 4b). As a consequence, the trend of water to stick to the SF is reduced, increasing the formed contact angle between SF and water. Hydrophobic behavior is also promoted by the increased surface roughness of SF membranes compared with SF films [39, 52]. As time increases, the contact angle between water and the different samples reduces to 0º due to the water absorption induced by the polar peptides of SF. This behavior is more noticeable in the measurements of the contact angle between electrolyte and SF. The results show that due to the mayor interactions between SF and the electrolyte solvents (ethylene carbonate and dimethyl carbonate) the samples are instantly fully wetted giving a contact angle of 0º. Comparing with other membranes as Celgard 2325, PP and PE with 52.0, 54.0 and 49.8 ° of EC/DMC $LiPF_6$ electrolyte contact angles [54], respectively, the prepared SF membranes show outstanding electrolyte wettability. The good electrolyte wettability with the membrane results in an increase of the lithium ion mobility and diffusion through the membrane, by the pathways created inside the membrane [55].

Figure 6b shows the electrolyte uptake measurements for the samples with porous structure (calculated from the eq. 1). The porosity is an essential factor in the performance of the battery separators since it allows the lithium ion mobility between the cathode and the anode. Comparing the three SF porous samples results it is possible to conclude that the samples with higher salt size (SF 250-106 μm) leads to a higher electrolyte uptake (350 %, after 5 min) than the other samples. The SF 38-22 μm and the SF 106-38 μm samples present almost the same uptake percentage after 5 min, 315 and 301 %, respectively. The high electrolyte uptake percentage of these samples compared with the conventional separator Celgard 2500 (125 %) [56], allows higher lithium ion transport pathways guaranteeing better electrochemical performance of the battery.

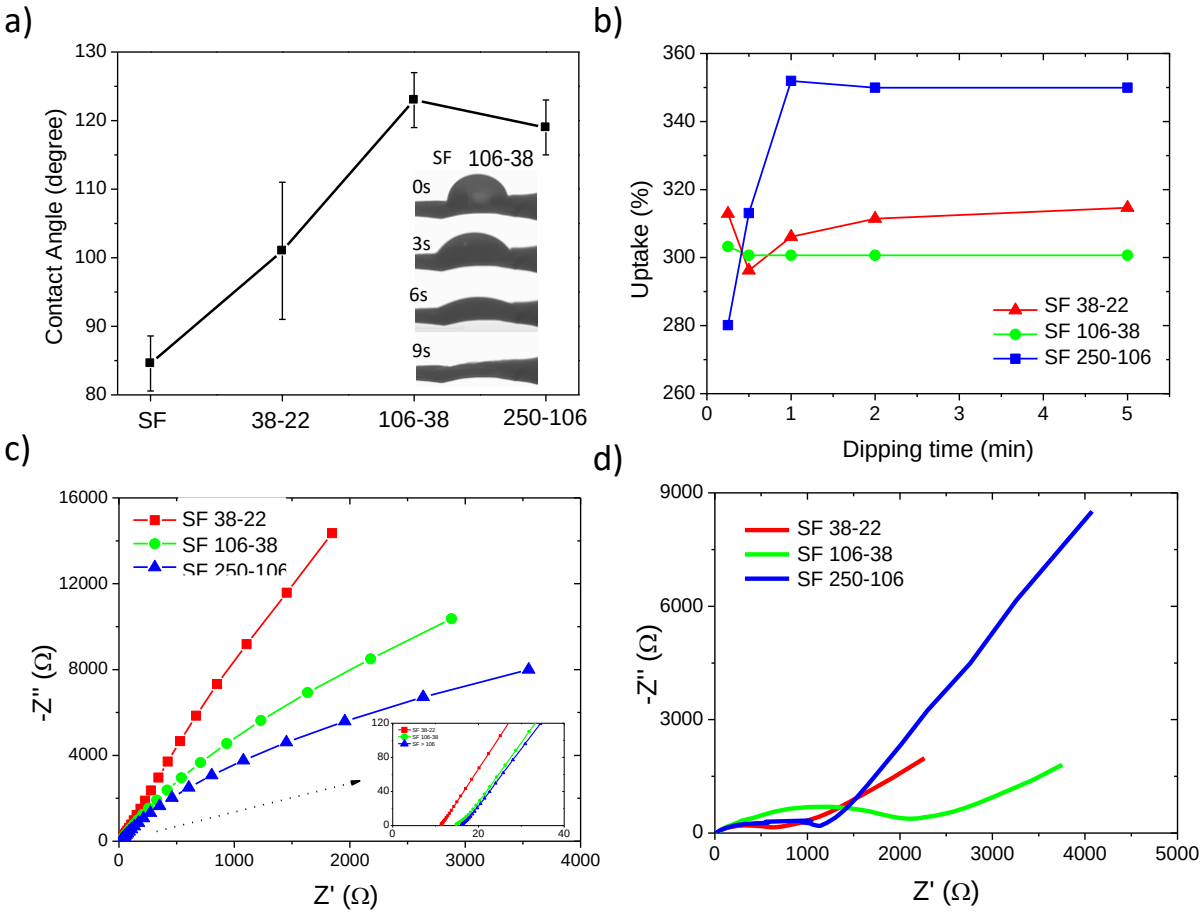


Figure 6 – a) Water contact angle, b) electrolyte uptake value as a function of time and c) Nyquist plot for the different membrane separators. d) Electrochemical impedance spectroscopy of the half-cell batteries with the different separators before cycling.

Electrochemical impedance spectroscopy (EIS) was performed for membranes previously soaked in the electrolyte and the corresponding results are presented in Figure 6c. The results show the presence of the typical behavior of electrolyte/electrode double layer capacitance due to the observed characteristic straight line. The interception of the high frequency value of the Nyquist plot with the Z´ gives the bulk resistance of the membranes and by eq. 2 the ionic conductivity (σ_i) can be obtained. Tortuosity (τ) and MacMullin number (N_M) of each sample were calculated by applying the eq. 3 and 4 respectively. The obtained data of ionic conductivity, tortuosity and MacMullin number were summarized in Table 2. The results show that the ionic conductivity is almost the same for all samples being the SF 38-22 μm the sample with highest ionic conductivity (2.5 $mS.cm^{-1}$). The ionic conductivity is higher than that reported in previous works [21] where SF membranes present ionic conductivity of 1 $mS \cdot cm^{-1}$, demonstrating that the microstructure and β-sheet percentage of SF membranes which can be controlled by salt leaching solvent casting method directly affect the ionic conductivity. The ionic conductivity value obtained in this work demonstrates being suitable for lithium ion battery systems that require a minimum of 10^{-1} $mS \cdot cm^{-1}$ [57]. The tortuosity and the MacMullin number also show values compatible with separator membranes leading to good battery performance [58].

Table 2 – Ion conductivity, tortuosity and MacMullin number calculated for the SF porous membranes.

Samples	**$\sigma_i \pm 0.3$ $mS.cm^{-1}$**	**$\tau \pm 0.2$**	**$N_M \pm 5\%$**
SF 38-22 μm	2.5	3.3	4.0
SF 106-38 μm	1.9	4.4	5.3
SF 250-106 μm	2.2	4.0	4.6

Impedance measurements of the SF membranes in half-cells, before cycling (Figure 6d), were performed to study the interfacial properties between the separator and the cathode. The Nyquist plot exhibit a semicircle in the high-medium frequency region and a linear at a low frequency region. The semicircle corresponds to the overall resistance, which is due to the ohmic, contact film and charge-transfer reaction resistances. The linear region designates the lithium ion diffusion in the cathode active material. The different SF membranes present overall resistances of 604, 2037 and 1134 Ω for SF 38-22 μm, SF 106-38 μm and SF 250-106 μm, respectively, the results indicating the formation and stabilization of the solid electrolyte interface (SEI) layer.

3.4. Battery performance

In order to evaluate the membranes performance as separator in lithium ion batteries, half-cells with the SF porous membranes were fabricated and the results are shown in Figure 7. Charge-discharge studies at different C rates (C/8, C/5, C/2, C and 2C) and charge-discharge cycles (55 cycles) at the same C rate were carried out at room temperature from 2.5 and 4.2 V. Figure 7a presents the fifth charge/discharge curve profiles at the studied C rates for the SF 38-22 μm membrane sample (all the samples present the same type of curve profile). The curves profiles are characterized by two voltages, one for the charge and other for the discharge. The charge is originated from the lithium removal and the discharge from the lithium insertion, phenomenon that occurs due to redox reactions Fe^{2+}/Fe^{3+} in the C-$LiFePO_4$ spinel, for all C rates [59]. It is observed a new plateau in the discharge curves at high scan rate above C that is explained by the volume change of the grain induced by the phase transformation between $LiFePO_4$ and $FePO_4$ [60]. Also, it is possible to verify that the cycling profile decreases with the increase of the C rate, excluding at C/8 that is slight lower than the C/5. This difference in capacity at the C/8 rate is explained by the ohmic polarization effect and by the formation of SEI at the first cycles. The discharge capacity values for the SF 38-22 μm membrane were 61.5, 94.9, 109.5, 122.0 and 119.9 $mAh.g^{-1}$ at 2C, C, C/2, C/5 and C/8 rates, respectively. The obtained results present excellent electrochemical values at C rates above C/2. Figure 7b presents the fifth charge/discharge curve at 2C and C/8 rates for all the three samples. The obtained voltage profile is very similar for all the samples. It was verified a small overpotential in the SF 250-106 μm sample (the charge capacity is higher than the discharge capacity). At both 2C and C/8 rates the sample with the highest charge/discharge capacity is the SF 250-106 μm (discharge capacities of 89.3 and 131.3 $mAh.g^{-1}$, for 2C and C/8 respectively). At 2C rate the SF 106-38 μm sample shows higher charge/discharge capacity value than SF 38-22 (discharge capacities of 64.1 and 61.6 $mAh.g^{-1}$, for SF 106-38 and SF 38-22 respectively). Otherwise, at C/8 rate, the SF 38-22 μm sample shows higher charge/discharge capacity value than SF 106-38. In this rate, the discharge capacity value is 111.3 and 119.9 $mAh.g^{-1}$, for SF 106-38 μm and SF 38-22 μm, respectively. Also, the discharge rate performance of the samples at the different rates from C/8 to 2C were evaluated (Figure 7c). It is observed that the SF 250-106 μm

sample shows the highest discharge capacity value verified for all C-rates followed by the SF 38-22 μm and SF 106-38 μm (excepting at 2C that SF 106-38 μm is higher than SF 38-22 μm). The membranes porosity, the uptake percentage and the β-sheet percentage characteristics of the samples are the main responsible for the charge/discharge capacity modification of the prepared batteries. The high porosity 250-106 μm, the uptake percentage of 350% and the β-sheet percentage of 65.9% lead to an enhancement of the electrochemical results. The high porosity and uptake percentage in the membrane leads to a higher number of pathways for the lithium ion transport, decreasing also the resistance [61]. Also, the high β-sheet percentage is correlated with the good electrochemical performance through the electroactive properties and polarity of this silk conformation [62]. Figure 7d shows the capacity retention of the discharge process of the batteries with the SF membranes, normalized to the C/8 rate, for the studied C-rates. The decrease of the capacity retention with the C-rate is observed and is attributed to the lithium diffusion phenomenon between the cathode and the separator [15]. At 2C, the SF 250-106 sample increases its capacity retention percentage with respect to the remainder samples, due to its high porosity that allows higher lithium diffusion [63].

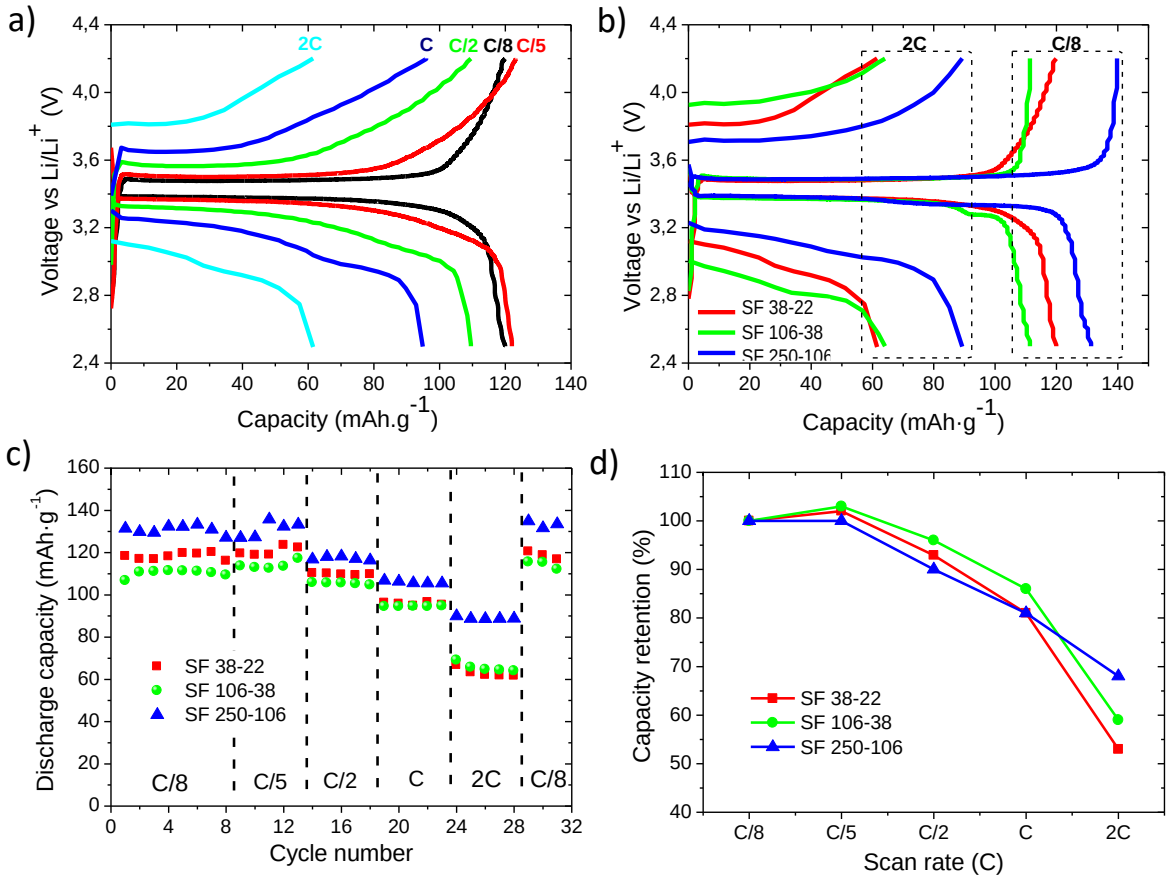


Figure 7 - a) Charge/discharge C-rates profiles for the SF 38-22 µm membrane battery. b) fifth charge/discharge curve 2C and C/8 rate, c) rate performance as a function of the cycle number and d) capacity retention for all the membranes in half-cell batteries.

The cycle performance and the coulombic efficiency percentage of the half-cell batteries prepared with the different membranes as separator were studied and the results are shown in Figure 8a. In this analysis, fifty-five cycles at C and 2C were performed and the discharge capacity obtained. After the 55 cycles, the discharge capacity at C was 89.2, 84.7 and 78.5 $mAh.g^{-1}$ and at 2C was 56.9, 38.0 and 22.4 $mAh.g^{-1}$, for the SF 250-106 µm, SF 38-22 µm and SF 106-28 µm membranes in the half-cells, respectively. The capacity retention obtained from the cycle performance were 86, 92 and 91% at C rate and 85, 79 and 84% at 2C rate, for the SF 250-106 µm, SF 38-22 µm and SF 106-28 µm membranes in the half-cells, respectively. The good cycling stability and capacity retention of the membranes is attributed to the higher uptake percentage value that correspond to a good swelling property of the membranes

and the high ionic conductivity. Also, all the membranes present a coulombic efficiency percentage around 100%, demonstrating to the good active species reversibility of the process during the charge and discharge. Figure 8b shows the impedance measurements of the half-cells with the SF membranes after cycling. The obtained overall resistances for SF 38-22 μm, SF 106-38 μm and SF 250-106 μm were 937.1, 2200.0 and 452.4 Ω, respectively. Comparing the previously obtained overall resistances before cycling (Figure 6b) and the after cycling, it is verified that the resistance increases in the half-cells after cycling, excepting in the SF 250-106 μm membrane where a stable SEI layer facilitates the lithium ion transport through the interface between the cathode and the separator. This result explains the better performance of the SF 250-106 μm, comparing with the other samples. In the other two samples, with lower surface area, the SEI layer reduce the lithium-ion diffusion after the cycling process, resulting a lower battery performance.

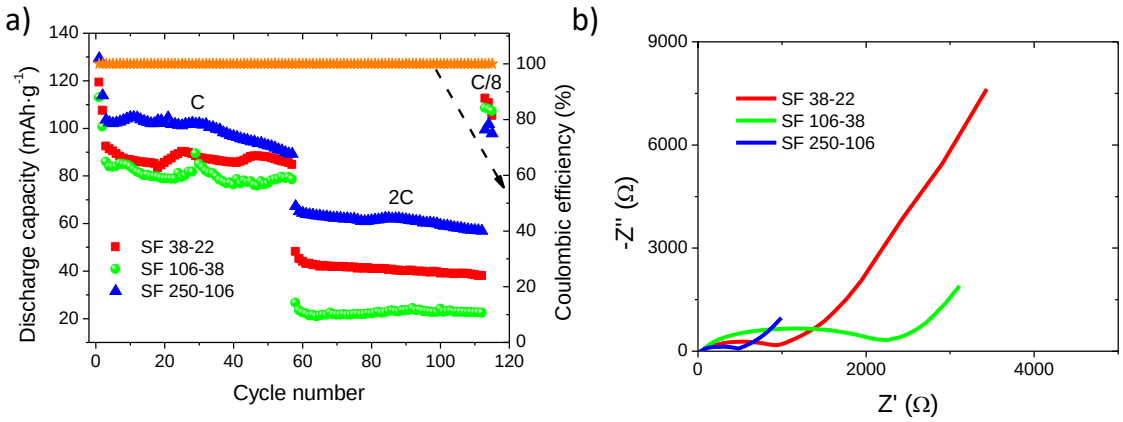


Figure 8 - a) Capacity and coulombic efficiency at C and 2C rates and b) electrochemical impedance spectroscopy after cycling, of the half-cell batteries prepared with the different separator membranes.

The obtained results can be compared with the ones obtained for different natural materials used as separators in lithium-ion batteries, as shown in Table 3.

Table 3 - Representative magnitudes of separator membranes from different natural polymers used in lithium-ion batteries.

Polymer	**Electrolyte Uptake / %**	**Porosity and Pore size / % and μm**	**σi / mS.cm^{-1}**	**Discharge capacity at 0.2C / mAh.g^{-1}**	**Ref**
Cellulose	-	-, <0.1	0.75	$LiCoO_2$ ≈ 138	[64]

nanofiber paper-derived - CNP (95/5 - IPA/water)					
Cross-linked cellulose membranes	542	-, -	6.34	NCM523 – 145	[65]
Cellulose pulp	275	70, -	108	$LiCoO_2$ – ≈ 130	[66]
Cellulose fibres from bleached softwood pulp (4 sheets)	425	73, -	1.5	Full battery $LiFePO_4$ ≈ 120	[67]
Cellulose-based composite nonwoven	270	70, 0.1-0.2	2	$LiCoO_2$ ≈ 129	[68]
Flexible egg shell membranes (ESM)	81	60, 1-5	0.1	$LiFePO_4$ - ≈ 75	[69]
Chitin nanofibers	242	40, 0.010-0.150	0.064	$LiFePO_4$ – 157 at 0.5C	[70]
Lignin	230	- , -	3.73	$LiFePO_4$ – 165	[71]
Rice paper	-	-, -	3 × celgard	$LiFePO_4$ ≈ 140 $LiCoO_2$ ≈ 130 $LiMn_2O_4$ ≈ 110	[72]
Bombyx mori Silkworm Cocoon	400	85, -	0.3	$LiFePO_4$ ≈ 131	[73]
Silk Fibroin prepared by lyophilization	1111	60, 150	1	$LiFePO_4$ ≈ 107	[21]
This work (SF 250-106)	350	90, 250-106	2.2	$LiFePO_4$ – 133.3	-

The importance of the use of natural materials in the area of energy storage in general and in lithium-ion batteries in particular is not just promising but also needed in the scope of developing sustainable technologies with reduced environmental impact. Materials such as cellulose (from different fonts), eggshell, chitin, lignin and silk have been used as lithium-ion separator membranes as shown in Table 3. The present work demonstrates that SF is a promising natural material, competitive with the aforementioned ones, to be used as separator due to their availability, electrochemical performance, ionic conductivity, chemical and thermal stability and easy porous control that allows to tune separator characteristics for improving battery performance.

4. Conclusions

The simple and environmental friendlier approach is presented in order to prepare silk fibroin (SF) based separator membranes with tailored pore size for lithium-ion batteries, an increasingly relevant research field for improving suitability and decrease environmental impact of energy storage systems. Different NaCl size salts (38-22, 38-106 and 250-106 μm) were used in order to obtain SF membranes by solvent evaporation with different average pore sizes. It is shown that the processing method does not change significantly the thermal and mechanical behavior of the membranes with respect to the SF films. On the other hand, the electrolyte uptake percentage is the highest for the SF 250-106 μm membranes (350 %, after 5 min) due to their higher pore size, leading to an ionic conductivity of 2.2 ± 0.3 mS cm^{-1}, suitable for battery applications. The relationship between β-sheet conformation percentage existing in the membrane and the pore size is evident, the β-sheet conformation content increasing with the average pore size. With respect to battery performance, the discharge capacity of half-cells prepared with SF 250-106 μm separators is 89.3 and 131.3 $mAh \cdot g^{-1}$, for 2C and C/8, respectively, a good performance when compared both with conventional and other natural materials-based separators. Further, the higher average pore size membranes, SF 250-106 μm, show the lowest overall resistance after cycling, a stable SEI layer facilitating the lithium-ion transport through the interface between the cathode and the separator that decreases the overall resistance. Thus, it is concluded that SF separator membranes with high porosity and tailored average pore size are suitable materials for lithium-ion battery separator membranes based on natural polymers, contributing to the green transition in the energy storage area.

Acknowledgements

The authors thank the FCT (Fundação para a Ciência e Tecnologia) for financial support under the framework of Strategic Funding grants UID/FIS/04650/2019, and UID/QUI/0686/2019 and project PTDC/FIS-MAC/28157/2017. The author also thanks the FCT for financial support under grant SFRH/BPD/112547/2015 (C.M.C.) and

Investigator FCT Contract CEECIND/00833/ 2017 (R.G.). Financial support from the Spanish Ministry of Economy and Competitiveness (MINECO) through project MAT2016-76039-C4-3-R (AEI/FEDER, UE) (including FEDER financial support) and from the Basque Government Industry and Education Departments under the ELKARTEK, HAZITEK and PIBA (PIBA-2018-06) programs, respectively, is also acknowledged

References

[1] J. Mohtasham, Review Article-Renewable Energies, Energy Procedia, 74 (2015) 1289-1297.

[2] Ş.E. Can Şener, J.L. Sharp, A. Anctil, Factors impacting diverging paths of renewable energy: A review, Renewable and Sustainable Energy Reviews, 81 (2018) 2335-2342.

[3] B. Diouf, R. Pode, Potential of lithium-ion batteries in renewable energy, Renewable Energy, 76 (2015) 375-380.

[4] J.B. Goodenough, K.-S. Park, The Li-Ion Rechargeable Battery: A Perspective, Journal of the American Chemical Society, 135 (2013) 1167-1176.

[5] B. Scrosati, J. Garche, Lithium batteries: Status, prospects and future, Journal of Power Sources, 195 (2010) 2419-2430.

[6] D.H.P. Kang, M. Chen, O.A. Ogunseitan, Potential Environmental and Human Health Impacts of Rechargeable Lithium Batteries in Electronic Waste, Environmental Science & Technology, 47 (2013) 5495-5503.

[7] Z. Chang, C. Li, Y. Wang, B. Chen, L. Fu, Y. Zhu, L. Zhang, Y. Wu, W. Huang, A lithium ion battery using an aqueous electrolyte solution, Scientific Reports, 6 (2016) 28421.

[8] N. Nitta, F. Wu, J.T. Lee, G. Yushin, Li-ion battery materials: present and future, Materials Today, 18 (2015) 252-264.

[9] C.M. Costa, M.M. Silva, S. Lanceros-Mendez, Battery separators based on vinylidene fluoride (VDF) polymers and copolymers for lithium ion battery applications, RSC Advances, 3 (2013) 11404-11417.

[10] Y. Wu, Lithium-Ion Batteries: Fundamentals and Applications, CRC Press, 2015.

[11] Z. Xue, D. He, X. Xie, Poly(ethylene oxide)-based electrolytes for lithium-ion batteries, Journal of Materials Chemistry A, 3 (2015) 19218-19253.

[12] K.M. Abraham, H.S. Choe, D.M. Pasquariello, Polyacrylonitrile electrolyte-based Li ion batteries, Electrochimica Acta, 43 (1998) 2399-2412.
[13] J.-H. Park, J.-H. Cho, W. Park, D. Ryoo, S.-J. Yoon, J.H. Kim, Y.U. Jeong, S.-Y. Lee, Close-packed SiO2/poly(methyl methacrylate) binary nanoparticles-coated polyethylene separators for lithium-ion batteries, Journal of Power Sources, 195 (2010) 8306-8310.
[14] M. Kundu, C.M. Costa, J. Dias, A. Maceiras, J.L. Vilas, S. Lanceros-Méndez, On the Relevance of the Polar β-Phase of Poly(vinylidene fluoride) for High Performance Lithium-Ion Battery Separators, The Journal of Physical Chemistry C, (2017).
[15] C.M. Costa, J.L. Gomez Ribelles, S. Lanceros-Méndez, G.B. Appetecchi, B. Scrosati, Poly(vinylidene fluoride)-based, co-polymer separator electrolyte membranes for lithium-ion battery systems, Journal of Power Sources, 245 (2014) 779-786.
[16] R.E. Sousa, J. Nunes-Pereira, C.M. Costa, M.M. Silva, S. Lanceros-Méndez, J. Hassoun, B. Scrosati, G.B. Appetecchi, Influence of the porosity degree of poly(vinylidene fluoride-co-hexafluoropropylene) separators in the performance of Li-ion batteries, Journal of Power Sources, 263 (2014) 29-36.
[17] R.E. Sousa, M. Kundu, A. Goren, M.M. Silva, L. Liu, C.M. Costa, S. Lanceros-Mendez, Poly(vinylidene fluoride-co-chlorotrifluoroethylene) (PVDF-CTFE) lithium-ion battery separator membranes prepared by phase inversion, RSC Advances, 5 (2015) 90428-90436.
[18] J. Sheng, S. Tong, Z. He, R. Yang, Recent developments of cellulose materials for lithium-ion battery separators, Cellulose, 24 (2017) 4103-4122.
[19] S.-D. Gong, Y. Huang, H.-J. Cao, Y.-H. Lin, Y. Li, S.-H. Tang, M.-S. Wang, X. Li, A green and environment-friendly gel polymer electrolyte with higher performances based on the natural matrix of lignin, Journal of Power Sources, 307 (2016) 624-633.
[20] S. Park, C.W. Son, S. Lee, D.Y. Kim, C. Park, K.S. Eom, T.F. Fuller, H.-I. Joh, S.M. Jo, Multicore-shell nanofiber architecture of polyimide/polyvinylidene fluoride blend for thermal and long-term stability of lithium ion battery separator, Scientific Reports, 6 (2016) 36977.
[21] R.F.P. Pereira, R. Brito-Pereira, R. Gonçalves, M.P. Silva, C.M. Costa, M.M. Silva, V. de Zea Bermudez, S. Lanceros-Méndez, Silk Fibroin Separators: A Step Toward Lithium-Ion Batteries with Enhanced Sustainability, ACS Applied Materials & Interfaces, 10 (2018) 5385-5394.

[22] L. Gaines, The future of automotive lithium-ion battery recycling: Charting a sustainable course, Sustainable Materials and Technologies, 1-2 (2014) 2-7.
[23] H. Zhang, J. Magoshi, M. Becker, J.Y. Chen, R. Matsunaga, Thermal properties of Bombyx mori silk fibers, Journal of Applied Polymer Science, 86 (2002) 1817-1820.
[24] Y. Cheng, L.-D. Koh, D. Li, B. Ji, M.-Y. Han, Y.-W. Zhang, On the strength of β-sheet crystallites of Bombyx mori silk fibroin, Journal of The Royal Society Interface, 11 (2014).
[25] S. Du, J. Zhang, W.T. Zhou, Q.X. Li, G.W. Greene, H.J. Zhu, J.L. Li, X.G. Wang, Interactions between fibroin and sericin proteins from Antheraea pernyi and Bombyx mori silk fibers, Journal of Colloid and Interface Science, 478 (2016) 316-323.
[26] A.U. Ude, R.A. Eshkoor, R. Zulkifili, A.K. Ariffin, A.W. Dzuraidah, C.H. Azhari, Bombyx mori silk fibre and its composite: A review of contemporary developments, Materials & Design, 57 (2014) 298-305.
[27] Y. Cao, B. Wang, Biodegradation of Silk Biomaterials, International Journal of Molecular Sciences, 10 (2009) 1514.
[28] X. Jia, C. Wang, C. Zhao, Y. Ge, G.G. Wallace, Toward Biodegradable Mg–Air Bioelectric Batteries Composed of Silk Fibroin–Polypyrrole Film, Advanced Functional Materials, 26 (2016) 1454-1462.
[29] J. Zhang, Y. Cai, Q. Zhong, D. Lai, J. Yao, Porous nitrogen-doped carbon derived from silk fibroin protein encapsulating sulfur as a superior cathode material for high-performance lithium–sulfur batteries, Nanoscale, 7 (2015) 17791-17797.
[30] X. Jia, C. Wang, V. Ranganathan, B. Napier, C. Yu, Y. Chao, M. Forsyth, F.G. Omenetto, D.R. MacFarlane, G.G. Wallace, A Biodegradable Thin-Film Magnesium Primary Battery Using Silk Fibroin–Ionic Liquid Polymer Electrolyte, ACS Energy Letters, 2 (2017) 831-836.
[31] T.-S. Kim, G.-H. Lee, S. Lee, Y.-S. Choi, J.-C. Kim, H.J. Song, D.-W. Kim, Carbon-decorated iron oxide hollow granules formed using a silk fibrous template: lithium-oxygen battery and wastewater treatment applications, Npg Asia Materials, 9 (2017) e450.
[32] J. Hou, C. Cao, F. Idrees, X. Ma, Hierarchical Porous Nitrogen-Doped Carbon Nanosheets Derived from Silk for Ultrahigh-Capacity Battery Anodes and Supercapacitors, ACS Nano, 9 (2015) 2556-2564.
[33] C.J. Weber, S. Geiger, S. Falusi, M. Roth, Material review of Li ion battery separators, AIP Conference Proceedings, 1597 (2014) 66-81.

[34] J.C. Barbosa, J.P. Dias, S. Lanceros-Méndez, C.M. Costa, Recent Advances in Poly(vinylidene fluoride) and Its Copolymers for Lithium-Ion Battery Separators, Membranes, 8 (2018) 45.

[35] A. Reizabal, D.M. Correia, C.M. Costa, L. Perez-Alvarez, J.L. Vilas-Vilela, S. Lanceros-Méndez, Silk Fibroin Bending Actuators as an Approach Toward Natural Polymer Based Active Materials, ACS Applied Materials & Interfaces, 11 (2019) 30197-30206.

[36] A. Maceiras, A. Gören, V. Sencadas, C.M. Costa, J.L. Vilas, S. Lanceros-Méndez, L.M. León, Effect of cyano dipolar groups on the performance of lithium-ion battery electrospun polyimide gel electrolyte membranes, Journal of Electroanalytical Chemistry, 778 (2016) 57-65.

[37] A. Gören, J. Mendes, H.M. Rodrigues, R.E. Sousa, J. Oliveira, L. Hilliou, C.M. Costa, M.M. Silva, S. Lanceros-Méndez, High performance screen-printed electrodes prepared by a green solvent approach for lithium-ion batteries, Journal of Power Sources, 334 (2016) 65-77.

[38] S. Lin-Gibson, J.A. Cooper, F.A. Landis, M.T. Cicerone, Systematic Investigation of Porogen Size and Content on Scaffold Morphometric Parameters and Properties, Biomacromolecules, 8 (2007) 1511-1518.

[39] A. Reizabal, S. Gonçalves, R. Brito-Pereira, P. Costa, C.M. Costa, L. Pérez-Álvarez, J.L. Vilas-Vilela, S. Lanceros-Méndez, Optimized silk fibroin piezoresistive nanocomposites for pressure sensing applications based on natural polymers, Nanoscale Advances, 1 (2019) 2284-2292.

[40] S. Ling, Z. Qi, D.P. Knight, Z. Shao, X. Chen, FTIR imaging, a useful method for studying the compatibility of silk fibroin-based polymer blends, Polymer Chemistry, 4 (2013) 5401-5406.

[41] W. Qiu, Y. Huang, W. Teng, C.M. Cohn, J. Cappello, X. Wu, Complete Recombinant Silk-Elastinlike Protein-Based Tissue Scaffold, Biomacromolecules, 11 (2010) 3219-3227.

[42] X. Hu, D. Kaplan, P. Cebe, Determining Beta-Sheet Crystallinity in Fibrous Proteins by Thermal Analysis and Infrared Spectroscopy, Macromolecules, 39 (2006) 6161-6170.

[43] J. Magoshi, Y. Magoshi, M.A. Becker, M. Kato, Z. Han, T. Tanaka, S.-i. Inoue, S. Nakamura, Crystallization of silk fibroin from solution, Thermochimica Acta, 352-353 (2000) 165-169.

[44] J.-J. Woo, Z. Zhang, N.L. Dietz Rago, W. Lu, K. Amine, A high performance separator with improved thermal stability for Li-ion batteries, Journal of Materials Chemistry A, 1 (2013) 8538-8540.
[45] J. Zhong, M. Ma, W. Li, J. Zhou, Z. Yan, D. He, Self-assembly of regenerated silk fibroin from random coil nanostructures to antiparallel β-sheet nanostructures, Biopolymers, 101 (2014) 1181-1192.
[46] E.S. Sashina, A.M. Bochek, N.P. Novoselov, D.A. Kirichenko, Structure and solubility of natural silk fibroin, Russian Journal of Applied Chemistry, 79 (2006) 869-876.
[47] N. Agarwal, D.A. Hoagland, R.J. Farris, Effect of moisture absorption on the thermal properties of Bombyx mori silk fibroin films, Journal of Applied Polymer Science, 63 (1997) 401-410.
[48] L.-D. Koh, Y. Cheng, C.-P. Teng, Y.-W. Khin, X.-J. Loh, S.-Y. Tee, M. Low, E. Ye, H.-D. Yu, Y.-W. Zhang, M.-Y. Han, Structures, mechanical properties and applications of silk fibroin materials, Progress in Polymer Science, 46 (2015) 86-110.
[49] G. Xu, G.W. Toh, N. Du, X.Y. Liu, Spider silk: The toughest natural polymer, RSC Green Chemistry, 1 (2012) 275-304.
[50] G. Xu, L. Gong, Z. Yang, X.Y. Liu, What makes spider silk fibers so strong? From molecular-crystallite network to hierarchical network structures, Soft Matter, 10 (2014) 2116-2123.
[51] J. Cannarella, X. Liu, C.Z. Leng, P.D. Sinko, G.Y. Gor, C.B. Arnold, Mechanical Properties of a Battery Separator under Compression and Tension, Journal of The Electrochemical Society, 161 (2014) F3117-F3122.
[52] J.T. Simpson, S.R. Hunter, T. Aytug, Superhydrophobic materials and coatings: a review, Reports on Progress in Physics, 78 (2015) 086501.
[53] Y. Qi, H. Wang, K. Wei, Y. Yang, R.-Y. Zheng, I.S. Kim, K.-Q. Zhang, A Review of Structure Construction of Silk Fibroin Biomaterials from Single Structures to Multi-Level Structures, International Journal of Molecular Sciences, 18 (2017) 237.
[54] M. Dahbi, D. Violleau, F. Ghamouss, J. Jacquemin, F. Tran-Van, D. Lemordant, M. Anouti, Interfacial Properties of LiTFSI and LiPF6-Based Electrolytes in Binary and Ternary Mixtures of Alkylcarbonates on Graphite Electrodes and Celgard Separator, Industrial & Engineering Chemistry Research, 51 (2012) 5240-5245.

[55] J.-A. Choi, S.H. Kim, D.-W. Kim, Enhancement of thermal stability and cycling performance in lithium-ion cells through the use of ceramic-coated separators, Journal of Power Sources, 195 (2010) 6192-6196.
[56] Y. Xie, H. Zou, H. Xiang, R. Xia, D. Liang, P. Shi, S. Dai, H. Wang, Enhancement on the wettability of lithium battery separator toward nonaqueous electrolytes, Journal of Membrane Science, 503 (2016) 25-30.
[57] J. Hassoun, D.-J. Lee, Y.-K. Sun, B. Scrosati, A lithium ion battery using nanostructured Sn–C anode, LiFePO4 cathode and polyethylene oxide-based electrolyte, Solid State Ionics, 202 (2011) 36-39.
[58] C.M. Costa, Y.-H. Lee, J.-H. Kim, S.-Y. Lee, S. Lanceros-Méndez, Recent advances on separator membranes for lithium-ion battery applications: From porous membranes to solid electrolytes, Energy Storage Materials, (2019).
[59] C. Fongy, A.-C. Gaillot, S. Jouanneau, D. Guyomard, B. Lestriez, Ionic vs Electronic Power Limitations and Analysis of the Fraction of Wired Grains in LiFePO4 Composite Electrodes, Journal of The Electrochemical Society, 157 (2010) A885-A891.
[60] J. Wu, W. Cai, G. Shang, In situ Electrochemical-AFM Study of LiFePO4 Thin Film in Aqueous Electrolyte, Nanoscale Research Letters, 11 (2016) 223.
[61] Y. Saito, W. Morimura, R. Kuratani, S. Nishikawa, Ion Transport in Separator Membranes of Lithium Secondary Batteries, The Journal of Physical Chemistry C, 119 (2015) 4702-4708.
[62] Z. Wang, Modeling and Simulation of Piezoelectrically Driven Self-Charging Lithium Ion Batteries, ACS Applied Materials & Interfaces, 9 (2017) 15893-15897.
[63] M. Singh, J. Kaiser, H. Hahn, Effect of Porosity on the Thick Electrodes for High Energy Density Lithium Ion Batteries for Stationary Applications, Batteries, 2 (2016) 35.
[64] S.-J. Chun, E.-S. Choi, E.-H. Lee, J.H. Kim, S.-Y. Lee, S.-Y. Lee, Eco-friendly cellulose nanofiber paper-derived separator membranes featuring tunable nanoporous network channels for lithium-ion batteries, Journal of Materials Chemistry, 22 (2012) 16618-16626.
[65] Z. Du, Y. Su, Y. Qu, L. Zhao, X. Jia, Y. Mo, F. Yu, J. Du, Y. Chen, A mechanically robust, biodegradable and high performance cellulose gel membrane as gel polymer electrolyte of lithium-ion battery, Electrochimica Acta, 299 (2019) 19-26.

[66] Q. Xu, Q. Kong, Z. Liu, J. Zhang, X. Wang, R. Liu, L. Yue, G. Cui, Polydopamine-coated cellulose microfibrillated membrane as high performance lithium-ion battery separator, RSC Advances, 4 (2014) 7845-7850.
[67] L. Zolin, M. Destro, D. Chaussy, N. Penazzi, C. Gerbaldi, D. Beneventi, Aqueous processing of paper separators by filtration dewatering: towards Li-ion paper batteries, Journal of Materials Chemistry A, 3 (2015) 14894-14901.
[68] J. Zhang, L. Yue, Q. Kong, Z. Liu, X. Zhou, C. Zhang, Q. Xu, B. Zhang, G. Ding, B. Qin, Y. Duan, Q. Wang, J. Yao, G. Cui, L. Chen, Sustainable, heat-resistant and flame-retardant cellulose-based composite separator for high-performance lithium ion battery, Scientific Reports, 4 (2014) 3935.
[69] M. Raja, A.M. Stephan, Natural, biodegradable and flexible egg shell membranes as separators for lithium-ion batteries, RSC Advances, 4 (2014) 58546-58552.
[70] T.-W. Zhang, B. Shen, H.-B. Yao, T. Ma, L.-L. Lu, F. Zhou, S.-H. Yu, Prawn Shell Derived Chitin Nanofiber Membranes as Advanced Sustainable Separators for Li/Na-Ion Batteries, Nano Letters, 17 (2017) 4894-4901.
[71] S.-D. Gong, Y. Huang, H.-J. Cao, Y.-H. Lin, Y. Li, S.-H. Tang, M.-S. Wang, X. Li, A green and environment-friendly gel polymer electrolyte with higher performances based on the natural matrix of lignin, Journal of Power Sources, 307 (2016) 624-633.
[72] L.C. Zhang, X. Sun, Z. Hu, C.C. Yuan, C.H. Chen, Rice paper as a separator membrane in lithium-ion batteries, Journal of Power Sources, 204 (2012) 149-154.
[73] R.F.P. Pereira, R. Gonçalves, M. Fernandes, C.M. Costa, M.M. Silva, V. de Zea Bermudez, S. Lanceros-Mendez, Bombyx mori Silkworm Cocoon Separators for Lithium-Ion Batteries with Superior Safety and Sustainability, Advanced Sustainable Systems, 2 (2018) 1800098.